



Removal of Toluene by Non-thermal Plasma Combined with $\text{Co}_x\text{Ni}_y\text{-MOF-74}$ Catalyst

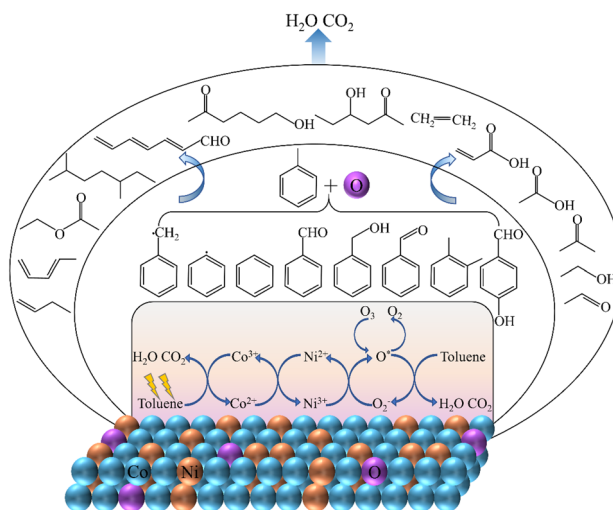
Youxiao Xu^{1,2} · Zhishuncheng Li^{1,2} · Guangfei Qu^{1,2} · Yiting Chen^{1,2} · Huanhuan Wu^{1,2} · Ping Ning^{1,2} · Junyan Li^{1,2}

Received: 19 July 2023 / Accepted: 21 September 2023 / Published online: 13 November 2023
© The Author(s), under exclusive licence to Springer Science+Business Media, LLC, part of Springer Nature 2023

Abstract

In this work, MOF-74 catalysts with various Co/Ni ratios obtained by hydrothermal method were prepared, and the degradation performance of various catalysts with synergistic non-thermal plasma for toluene was investigated. The addition of catalysts to NTP shown notable effects in toluene degradation and energy usage efficiency when compared to NTP alone. Notably, $\text{Co}_x\text{Ni}_y\text{-MOF}$ outperformed Co-MOF and Ni-MOF in terms of toluene catalytic activity. In comparison to the single plasma condition, $\text{Co}_2\text{Ni}_3\text{-MOF}$ showed the maximum toluene degradation rate of 78% at the NTP discharge power of 11.66 W. SEM, BET, XRD, XPS, and FTIR were used to examine the impact of various Co/Ni ratios on the structure and redox characteristics of the samples. The interaction of Co and Ni results in many flaws and oxygen vacancies, increasing the amount of oxygen adsorbed on the surface and the reducibility of the catalyst, which is thought to be the cause of the rise in catalytic activity. Finally, based on the discovered organic compounds, the process of toluene breakdown in the plasma co-catalytic system was deduced. This work provides a novel concept for improving catalysts for the non-thermal plasma-catalyzed decomposition of toluene.

Graphical Abstract



Keywords Non-thermal plasma · Toluene degradation · MOF-74 · Catalytic oxidation · Reaction mechanism

1 Introduction

The acceleration of industrialization and urbanization in recent years has resulted in a remarkable increase in annual emissions of volatile organic compounds (VOCs). The

main sources of air pollutants are VOCs generated by the chemical industry, textile production, interior products, and transportation, which pose a significant threat to the ecological environment as well as human health and safety [1, 2]. Traditional VOCs treatment methods include absorption methods [3], adsorption method [4], membrane separation method [5], combustion method [6], photocatalytic method [7], biodegradation method [8] and other methods. Although these methods are commonly used in industrial production, these treatment methods have certain drawbacks in terms of cost and degradation efficiency.

Non-thermal plasma (NTP) is rapidly developing in the purification of VOCs, especially for low concentration and complex VOCs with unique advantages [9]. According to the various discharge forms, NTP can be divided into corona discharge, dielectric barrier discharge, glow discharge, radio frequency discharge, microwave discharge, and atomized corona discharge [10–12]. Dielectric barrier discharge and corona discharge are being employed extensively in the study and treatment of VOCs due to their low initial investment, convenient operation, and low energy consumption.

The NTP degradation of VOCs is a very complex process where the chemical reaction occurs mainly in the plasma discharge of high-energy electrons (1–10 eV) and gas molecules collision, resulting in highly reactive substances, such as ions, free radicals, excited atoms and molecules, which collide with the gas molecules, breaking the molecular bonds between the molecules [13, 14]. Thus, thermodynamically and/or kinetically unfavorable reactions occur under mild conditions [15]. However, the single NTP approach has issues including low energy usage, low mineralization, and ease of producing harmful by-products to form secondary pollution, thus the applicability on a broad scale is constrained [16]. So, a novel method of treating VOCs that combines multiphase catalysis with NTP has been suggested. Both post-plasma catalysis (PPC), where the catalyst is positioned upstream of the plasma discharge zone, and in-plasma catalysis (IPC), where the catalyst is positioned in the plasma discharge region, are possible configurations for this NTP-catalysis system. Typically, IPC may achieve great energy efficiency and higher VOC degradation efficiency [17]. However, the location of the catalyst in the discharge zone may have an impact on the amount and kind of discharge as well as the catalyst's quick deactivation, leading to an unstable discharge. In PPC, the possibility of catalyst deactivation may be decreased while the influence of the catalyst on discharge stability can be effectively avoided. Additionally, replacing old catalysts in real-world applications is made simpler by the fact that PPC systems are easier to setup than IPC systems [18, 19].

The effectiveness of NTP catalytic systems with PPC structure is significantly influenced by the catalyst selection. Metal–organic frameworks (MOFs) are a type of

porous crystalline material generated by the coordination interactions of metal ions or metal clusters with organic ligands [20]. MOFs, as an organic–inorganic hybrid material, have benefits such as a rich structure, ultra-high specific surface area, homogeneous nanoscale cavities, ultra-high porosity, strong thermal stability, and chemical characteristics [21]. It has been widely used in gas adsorption and separation, non-homogeneous catalysis, drug delivery, luminescence and sensing, etc. [22–29]. Notably, the customizability of the backbone makes it easy to modify the metal sites and organic groups in MOFs, giving them unique catalytic properties [30]. Currently, there are some MOFs that have been studied in the field of VOCs elimination. For example, Li et al. developed and synthesized Pt/Uio-66NPs for catalytic oxidation of several VOCs and discovered that ethyl acetate (260 °C), n-hexane (260 °C), and toluene (180 °C) had near to 100% conversion efficiencies and CO₂ yields. It also demonstrated great reusability, water resistance, and outstanding stability for more than 150 h [31]. Similarly, Li et al. synthesized TiO₂@ZIF-8 metal nanoparticles with a stable prismatic dodecahedral structure. Used for NTP removal of toluene, research results show that the load is 10% TiO₂@ZIF-8. The maximum toluene conversion efficiency of the catalyst is 93.57%, the CO_x selectivity is 79.38%, and the O₃ decomposition efficiency is 99.22%. The catalyst still maintains high catalytic activity after 36 h of stability testing [32]. This is due to the superior adsorption capabilities of MOFs, which may absorb toluene in their porous structure, lengthen toluene's residence time in the reaction system, enhance the chance of intermolecular collisions, and therefore boost degradation efficiency. The collaboration of various metals can improve the collection of VOCs and modify the energy barriers of reaction intermediates in addition to the synergistic catalytic impact of metal sites and organic groups [33, 34]. Rong and colleagues discovered that the synergistic plasma-catalyzed degradation of toluene by Mn/Ce bimetallic MOFs considerably increased the catalytic efficiency, energy efficiency, and CO₂ selectivity of toluene, and that the by-product O₃ emission concentration was dramatically decreased [35].

MOF-74 is a honeycomb material with a pore size of roughly 12 nm that is made by mixing divalent metal ions with 2,5-dihydroxyterephthalic acid. The geometry of the metal nodes can be changed from the original saturated six-ligand octahedral configuration to an unsaturated five-ligand tetragonal pyramidal configuration by heating and desorption of solvent molecules, resulting in an open unsaturated metal site that can be used for catalytic reactions [36]. Among these, Co-MOF-74 exhibits excellent potential for eliminating VOCs. Liao et al. used a hydrothermal technique to create a MOF catalyst Co₃O₄-M-3 with a 3D homogenous spherical shape that demonstrated the highest degradation

efficiency (92%) in photocatalytic oxidation of ethyl acetate [37].

In this work, hydrothermal Co_xNi_y-MOF catalysts with various Co/Ni ratios were created and used in the toluene corona discharge plasma co-catalytic degradation system. The toluene removal rate, energy efficiency, O₃ concentration, and selectivity of the total gas-phase intermediate products were used to assess the effectiveness of the plasma co-MOFs catalysts for toluene degradation. Powder X-ray diffraction (XRD), low-temperature N₂ adsorption, X-ray photoelectron spectroscopy (XPS), scanning electron microscopy (SEM), and other techniques were used to analyze the produced materials. By identifying and analyzing the organic by-products in the degradation tail gas using gas chromatography (GC), the reaction mechanism of toluene degradation over CoNi-MOF catalyst under plasma discharge strips was presented.

2 Experimental

2.1 Experimental Setup

The experimental system for NTP co-catalytic toluene degradation consists primarily of the following components: gas delivery system, corona discharge plasma reaction system, catalyst performance assessment system, and exhaust gas monitoring system, among others. The schematic diagram of the device is shown in Fig. 1. (1) Gas distribution system: The syringe pump injects liquid toluene into the three-port flask (which is placed in an 85 °C constant temperature water bath), and the dry air flowing through the gas bottle enters the three-port flask and mixes with the volatile toluene vapor to form the toluene-containing airflow. Syringe pump advance rate and gas flow are used in combination to regulate toluene concentration. (2) Corona discharge plasma reaction system: for plasma discharge, a handmade high-voltage DC power supply with a discharge voltage range of 0–50 kV and a current range of 0–5 mA is employed.

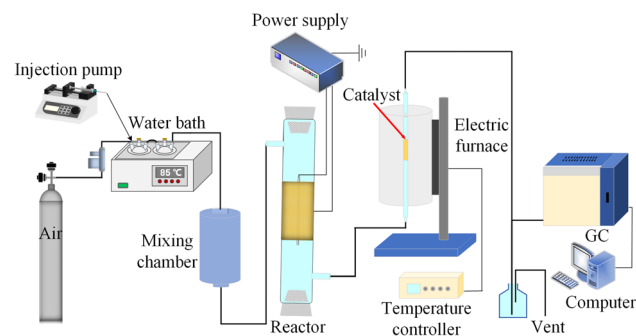


Fig. 1 Flow chart of the experimental setup

The plasma reactor is a homemade concentric circular tube structure, with the outer electrode being a stainless steel circular tube with a diameter of 39 mm and a length of 120 mm, the inner electrode being a stainless steel circular rod with a diameter of 2 mm and a length of 120 mm, and the outer electrode being a transparent quartz tube with inlets and outlets on both ends. A transparent quartz tube with inlet and outflow ports is used as the exterior electrode surface. The catalytic reactor is located at the back end of the plasma reactor in the post-plasma catalytic reaction system. (3) Catalyst performance evaluation system: 1 g of powder catalyst was diluted (1:3) with quartz sand and placed in a quartz tube with an inner diameter of 7 mm. The quartz tube was inserted in a tube furnace after the catalytic region was repaired with quartz wool. For the assessment of the plasma toluene pretreatment-post-catalysis experiment in this work, the tube furnace temperature was set at 200 °C, and the toluene conversion was only determined after 30 min of steady state. (4) Exhaust gas detection system: A hydrogen flame ionization detector (FID)-equipped gas chromatography (GC 1120) system is used to determine the toluene content in the outflow gas.

2.2 Catalyst Preparation

The hydrothermal approach was used to produce the MOFs catalysts as follows [38]: first, 2,5-dihydroxyterephthalic acid was dissolved in a 75 mL combination of DMF, ethanol, and H₂O in a 1:1:1 ratio. Then add Co(NO₃)₂·6H₂O and Ni(NO₃)₂·6H₂O in the ratio of 1:0, 1:1, 2:3, 3:2, 0:1 to the mixed solution, and sonicate for 30 min until the solid material is completely dissolved, Then the mixed solution was transferred to a 100 ml reactor and reacted at 110 °C for 24 h. After the reactor cooled down to room temperature, the solution was separated by centrifugation to obtain solid material and washed with ethanol and deionized water for three times, and finally the solid product was dried in a vacuum oven at 90 °C for 12 h. The dried powder catalyst was prepared into 40–60 mesh particles and sealed for use.

2.3 Characterization of the Catalyst

The XRD patterns of the samples were recorded on a Rigaku Ultima IV diffractometer using Cu K α X-ray radiation with a 0.02° step size over the 2-theta range: 10°–90°. The morphology and structure of the catalyst surface were analyzed using a TESCAN MIRA LMS scanning electron microscope. Micromeritics ASAP2460 specific surface and porosity analyzer was used to examine the catalysts' specific surface area and pore structure. Before testing, the samples were degassed for 3 h and then tested at 77 K with N₂ as the adsorbent gas. Following the completion of the testing, the specific surface area of the samples was estimated

using Brunauer-Emmiett-Teller (BET). XPS with a monochromatic Al K α source was employed to study the surface properties and valence state distribution (Thermo Scientific K-Alpha), and the C 1s level at 284.8 eV was regarded as an internal standard to revise the shift of the binding energy due to relative surface charging. The phase species and surface groups of the catalysts were investigated using a Bruker Tensor 27 FTIR analyzer. The infrared spectra were scanned in the 500–4000 cm⁻¹ wavenumber range.

2.4 Analysis Method

Toluene degradation is assessed simultaneously by toluene removal rate and energy efficiency, which are computed as follows.

$$SIE = \frac{60UI}{Q}$$

$$\eta_{C_7H_8} \% = \frac{[C_7H_8]_{in} - [C_7H_8]_{out}}{[C_7H_8]_{in}} \times 100$$

$$\eta_{EY} gkWh^{-1} = \frac{3.6 \times M_{C_7H_8} \times ([C_7H_8]_{in} - [C_7H_8]_{out})}{22.4 \times SIE}$$

where U is the applied voltage, I is the corresponding current, Q is the reaction gas flow rate (L min⁻¹), [C₇H₈]_{in} and [C₇H₈]_{out} are the initial toluene concentration and the

toluene concentration at the reactor outlet (mg m⁻³), respectively, and M is the relative molecular mass of toluene (g mol⁻¹).

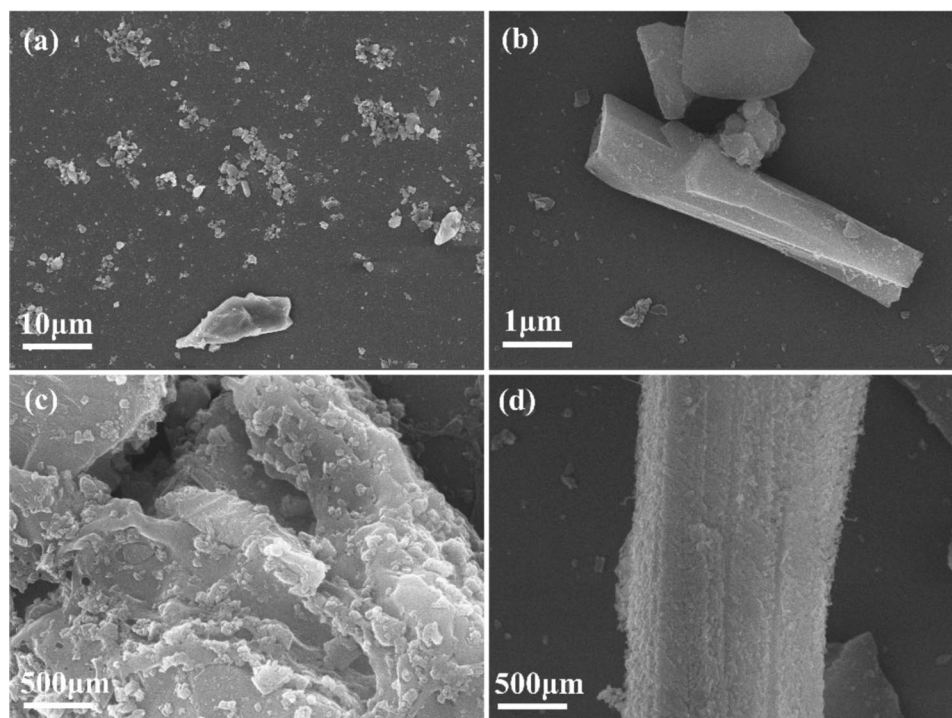
3 Results and Discussion

3.1 Catalyst Characterization

In order to gain insight into the morphology and microstructure of the obtained MOFs, scanning electron microscopy of the Co₂Ni₃-MOF catalysts was performed as shown in Fig. 2. And in Fig. 2a, b, it can be seen that MOF nanoparticles have a clustered structure and a one-dimensional micrometer rod-like structure. Under high magnification, Fig. 2c shows the existence of a microporous structure on the surface and metal particles stuck close to the microporous; Fig. 2d shows evenly dispersed nanoflakes on the surface of the synthesized MOFs. The synthesized material has the same structure as reported in the literature [39].

Nitrogen adsorption was used to examine the porosity and specific surface area of the Co_xNi_y-MOF-74 catalyst. The N₂ adsorption–desorption isotherms of the MOF catalysts are depicted in Fig. 3a. The isotherm of this form of MOF is type IV, according to the IUPAC isotherm shape classification, indicating the presence of structural pores, interparticle mesopores, and macropores [40]. Table 1 displays the BET specific surface area (S_{BET}), pore size (D_p), and total pore volume (V_t) of the produced materials. The Co₂Ni₃-MOF

Fig. 2 SEM images of Co₂Ni₃-MOF catalysts at different magnifications. **a** 10 μ m, **b** 1 μ m, **c** 500 μ m, **d** 500 μ m, and **e** 10 μ m



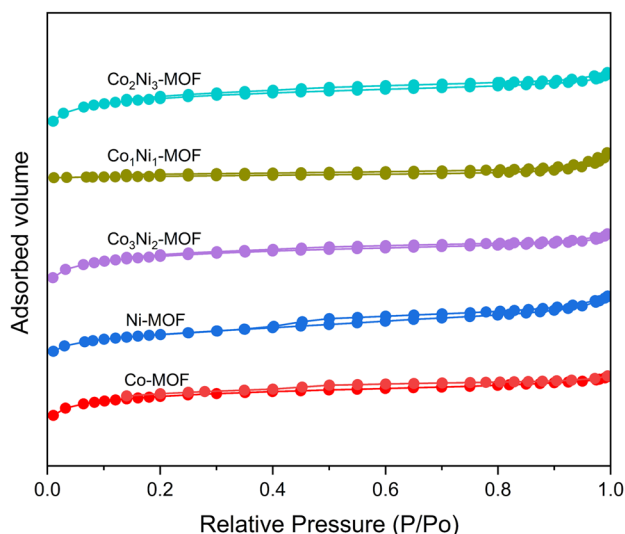


Fig. 3 N₂ adsorption–desorption isotherms of synthesized catalysts

Table 1 Pore structure characteristics of the materials

Catalyst	S _{BET} /(m ² g ⁻¹)	V _{total} /(cm ³ g ⁻¹)	Pore diameter Dv(d)/(cm ³ g ⁻¹)
Co-MOF	844.14	0.43	38.69
Ni-MOF	306.40	0.19	44.8
Co ₃ Ni ₂ -MOF	829.51	0.44	41.1
Co ₁ Ni ₁ -MOF	823.65	0.42	40.29
Co ₂ Ni ₃ -MOF	915.12	0.47	41.29

material was found to possess the largest specific surface area of 915.12 m² g⁻¹, which is consistent with the conclusion that the MOF material has a high specific surface area, proving the successful synthesis of the MOF material. MOF material has a high specific surface area and demonstrates the effective synthesis of the MOF material. The low specific surface area, pore size and total pore capacity of Ni-MOF-74 catalysts may be due to the inadequate reaction during the synthesis of the material. The higher specific surface area facilitates the formation of more surface oxygen vacancies. It can be speculated that the Co₂Ni₃-MOF catalyst may have more surface oxygen vacancies. In addition, the pore size and total pore capacity of Co₂Ni₃-MOF are also the largest, which will facilitate the adsorption of gases on its surface, and the increase of pore size can provide more reaction sites to improve the catalytic activity.

To further establish the structure of the catalysts, FTIR spectra of all synthesized materials were obtained in this experiment, as shown in Fig. 4, with all samples exhibiting comparable characteristic peaks, showing the presence of the same functional groups. The stretching vibration of -OH corresponds to the broad and strong absorption peak

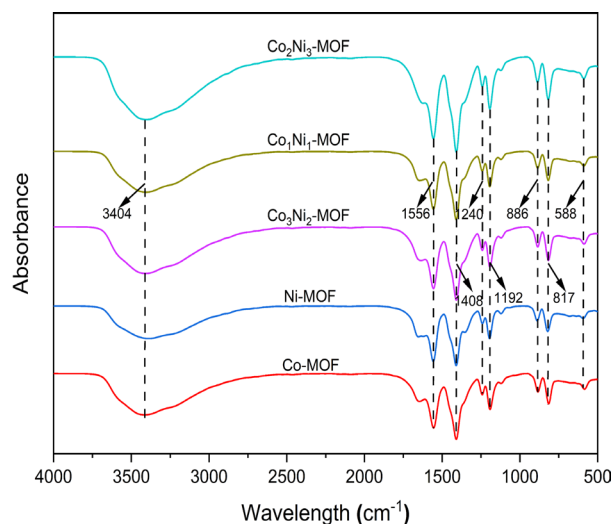


Fig. 4 FTIR spectra of different catalysts

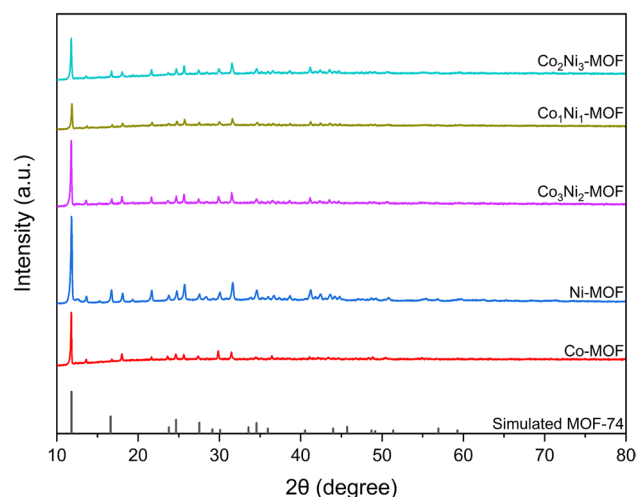


Fig. 5 XRD spectrum of catalysts

at 3404 cm⁻¹, confirming the presence of intramolecular hydrogen bonds in CoNi-MOF. C=O in the ligand and C=C stretching vibrations in the benzene ring skeleton are responsible for the absorption peaks at 1556 and 1408 cm⁻¹ [41]. The typical vibrational peaks of C–O and C–H appear at 1240 and 1192 cm⁻¹, respectively. In addition, the absorption peaks at 886 and 817 cm⁻¹ are bending vibrations beyond the C=C–H bond on the benzene ring. The peak at 588 cm⁻¹ belongs to the stretching vibrations of metal ions and oxygen (M–O) [42].

The samples were subjected to XRD analysis to establish their phase purity and crystal structure. As depicted in Fig. 5, all of the samples had distinct and crisp diffraction peaks. The generated Co-MOF, Ni-MOF, and Co_xNi_y-MOF (x/y = 1:1, 2:3, and 3:2) have similar crystal structures,

according to the XRD patterns. Characteristic peaks belonging to MOF were observed at 11.8°, 16.6°, 18.1° and 27.5°, indicating the successful synthesis of highly crystalline samples. It's also consistent with previous reports [43]. It is interesting to observe that the doping of Ni did not alter the crystalline structure of MOF, which may be related to the identical electrical valence and coordination environments between Co^{2+} and Ni^{2+} [44].

XPS was used to analyze the Co_2Ni_3 -MOF catalysts before and after the catalytic reaction in order to determine the surface chemical valence and composition of the catalysts. It should be mentioned that C 1s with a binding energy of 284.8 eV were used to calibrate all binding energies. The prepared Co_2Ni_3 -MOF includes elements including Co, Ni, C, and O, as illustrated in Fig. 6a. After the reaction, the elements Co and Ni are enhanced whereas the elements C and N are much less abundant than the pre-reaction material. Compared with pristine CoNi-MOF, it is shown that the catalytic process leads to partial detachment and corrosion of the distributor.

Furthermore, as shown in Fig. 6b, the high-resolution spectra of Ni $2p_{3/2}$ and Ni $2p_{1/2}$ split into two spin-orbit bimodal patterns, which are attributed to Ni^{2+} (873.2 and 855.6 eV) and Ni^{3+} (874.8 and 857.1 eV) [45]. The other two peaks at 879.5 and 861.1 eV are satellite peaks, respectively. The Co 2p spectra of Co $2p_{3/2}$ and Co $2p_{1/2}$ (Fig. 6c) are divided into two spin-orbit bimodal features attributed to Co^{2+} (798.0 and 782.6 eV) and Co^{3+} (796.4 and 780.7 eV) [46], and satellite peaks at 802.1 and 786.0 eV. The presence of Co^{3+} and Ni^{3+} may be owing to the slight oxidation of these divalent metal ions during preparation at room temperature and relative humidity [39]. Peaks at 284.8, 286.0, 288.5, and 289.4 eV in Fig. 6d for C 1s correspond to C–C, C–OH, C=O, and C(O)O organic ligands, respectively. After the reaction, there were no changes in the intensity or location of the C 1s characteristic peaks. It has been shown that the Co_2Ni_3 -MOF material has outstanding stability. The O 1s spectra before and after the reaction are shown in Fig. 6e, where the O 1sXPS spectrum of the sample can be convolved to integrate three peaks centered at 531.3, 532.0, and 533.1 eV, which are associated to the catalyst surface lattice oxygen (O_{lat}), surface adsorbed oxygen (O_{sur}), and hydroxyl oxygen or carbonate oxygen (O_{ads} , $-\text{OH}$, or CO_2^{3-}) [47].

The relative concentrations of $\text{Co}^{3+}/(\text{Co}^{3+} + \text{Co}^{2+})$ on the surface of the Co_2Ni_3 -MOF material were approximately 58.15 and 33.32% before and after the reaction, respectively, and the relative concentrations of $\text{Ni}^{3+}/(\text{Ni}^{3+} + \text{Ni}^{2+})$ on the surface were 59.50 and 35.39%, respectively, according to the quantitative analysis results shown in Table 2. Indicating that Co^{3+} and Ni^{3+} play a prominent role in the catalytic reaction is the decrease in the content of Co^{3+} and Ni^{3+} ions in the high valence state [48]. It has been reported that when the amount of high valence metal ions drops, so does the

chemical potential of the catalyst and the reactivity of oxygen next to the metal ions [49]. And more reactive oxygen species are introduced at higher valence states, which are connected to catalytic activity [50]. As a result, it can be demonstrated that the catalyst's catalytic activity decreases following the reaction. It is clear from the results of the semi-quantitative analysis of the oxygen species that $\text{O}_{\text{lat}}/\text{O}_{\text{sur}}$ increased before the reaction compared to after the reaction, and the content of O_{ads} after the reaction was higher than before the reaction as a result, confirming the change in oxygen mobility during the reaction. This is thought to favor a two-stage redox process (Mars-van-Krevelen mechanism) for oxidizing VOCs [51].

3.2 Catalytic Activity

At a toluene concentration of 822.68 mg m^{-3} , a gas flow rate of 200 ml min^{-1} , and a tube furnace heating temperature of 200 °C, the catalytic degradation performance of five MOFs catalysts for toluene degradation was investigated in this experiment. The performance of the plasma synergistic MOFs catalysts for toluene degradation was evaluated in terms of toluene removal, energy efficiency, O_3 concentration and total gas-phase intermediate product selectivity.

The impact of plasma discharge power on toluene conversion using various MOFs catalysts is depicted in Fig. 7a. Under all test settings, the toluene removal efficiency increased steadily as the plasma discharge power increased from roughly 1.61 to 11.664 W. This can be explained by the increased input power producing more energetic reactive species, which causes more collisions between the reactive particles and toluene, accelerating the breakdown of VOCs [52]. Notably, in the plasma co-catalyzed degradation of toluene system, Co_xNi_y -MOF shown superior catalytic activity for toluene than Co-MOF and Ni-MOF. Additionally, the oxidation of toluene by Co_xNi_y -MOF catalysts with various Co/Ni molar ratios revealed noticeable variations. Among them, Co_2Ni_3 -MOF demonstrated the greatest catalytic performance and the maximum energy efficiency for toluene oxidation. The greatest toluene degradation rate was 78% at a plasma discharge power of 11.66 W, although the degradation efficiency was only 37.2% for a single plasma condition, which was 52.3% higher than without the catalyst. The toluene degradation efficiency of the plasma-catalyzed system containing MOFs was graded as follows under the same operating conditions: Co_2Ni_3 -MOF > Co_1Ni_1 -MOF > Co_3Ni_2 -MOF > Ni-MOF > Co-MOF > NTP. The synergistic impact between the bimetallic particles is demonstrated by the fact that all of the degrading properties of the bimetallic MOFs materials are higher than those of the single-component Co/Ni-MOFs.

The variation of energy efficiency with plasma discharge power for different MOFs catalysts is given in Fig. 7b. The

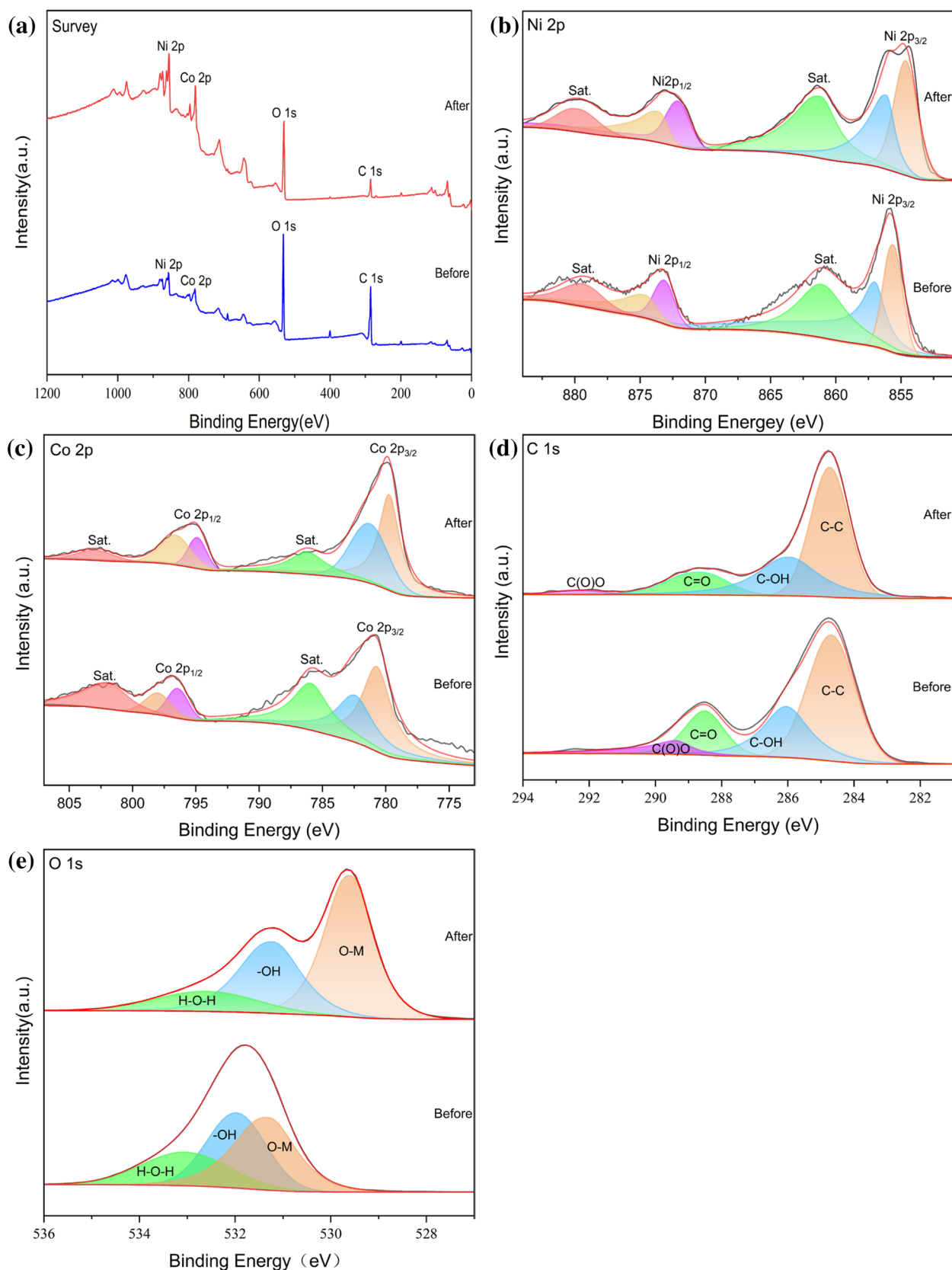


Fig. 6 XPS pattern of $\text{Co}_2\text{Ni}_3\text{-MOF-74}$. **a** Survey, **b** C 1s, **c** O 1s, **d** Ni 2p and **e** Co 2p

Table 2 XPS results of synthesized catalysts

Catalysts	Co ³⁺ / (Co ³⁺ + Co ²⁺) (%)	Ni ³⁺ / (Ni ³⁺ + Ni ²⁺) (%)	Olat/Osur (ratio)	Oads/Ototal (%)
Before	58.15	59.50	1.10	12.98
After	33.32	35.39	1.51	15.13

energy efficiency of the plasma co-catalytic system is better than that of the solitary plasma, as can be shown. This is because the active material created by the plasma discharge may reach and act on the catalyst surface, enhancing energy consumption. Comparing the energy efficiencies at the highest toluene degradation rate, the energy efficiency of NTP increased from 91.7 to 117.7 g kWh⁻¹, while the energy efficiency decreased from 1100.7 to 246.8 g kWh⁻¹ in the presence of Co₂Ni₃-MOF catalyst. The energy efficiency decreases as input power rises because, despite a significant

increase in the amount of active material produced, only a small portion of the active material is actually used in the degradation of toluene; instead, the majority of the active material is lost as heat. Even while raising the input power enhances the degrading efficiency even more, the energy consumption also rises, decreasing the reaction's economics.

Figure 7c depicts the fluctuation in O₃ concentration recorded at the tail gas output for toluene breakdown using various catalysts. The highest O₃ concentration (741 ppm) can be detected at the exhaust gas outlet in the case of toluene degradation by plasma alone, but the O₃ concentration is clearly reduced in the system of toluene degradation by plasma in combination with the MOF-74 catalyst.

The GC spectrum of the toluene degradation products from the plasma synergistic MOF-74 catalyst is shown in Fig. 8. The principal chemicals found in the exhaust gas that was discovered were acetic acid, acetone, ethyl acetate, benzene, toluene, and benzoic acid. Due to their low content, several of the goods were not discovered. Co₂Ni₃-MOF

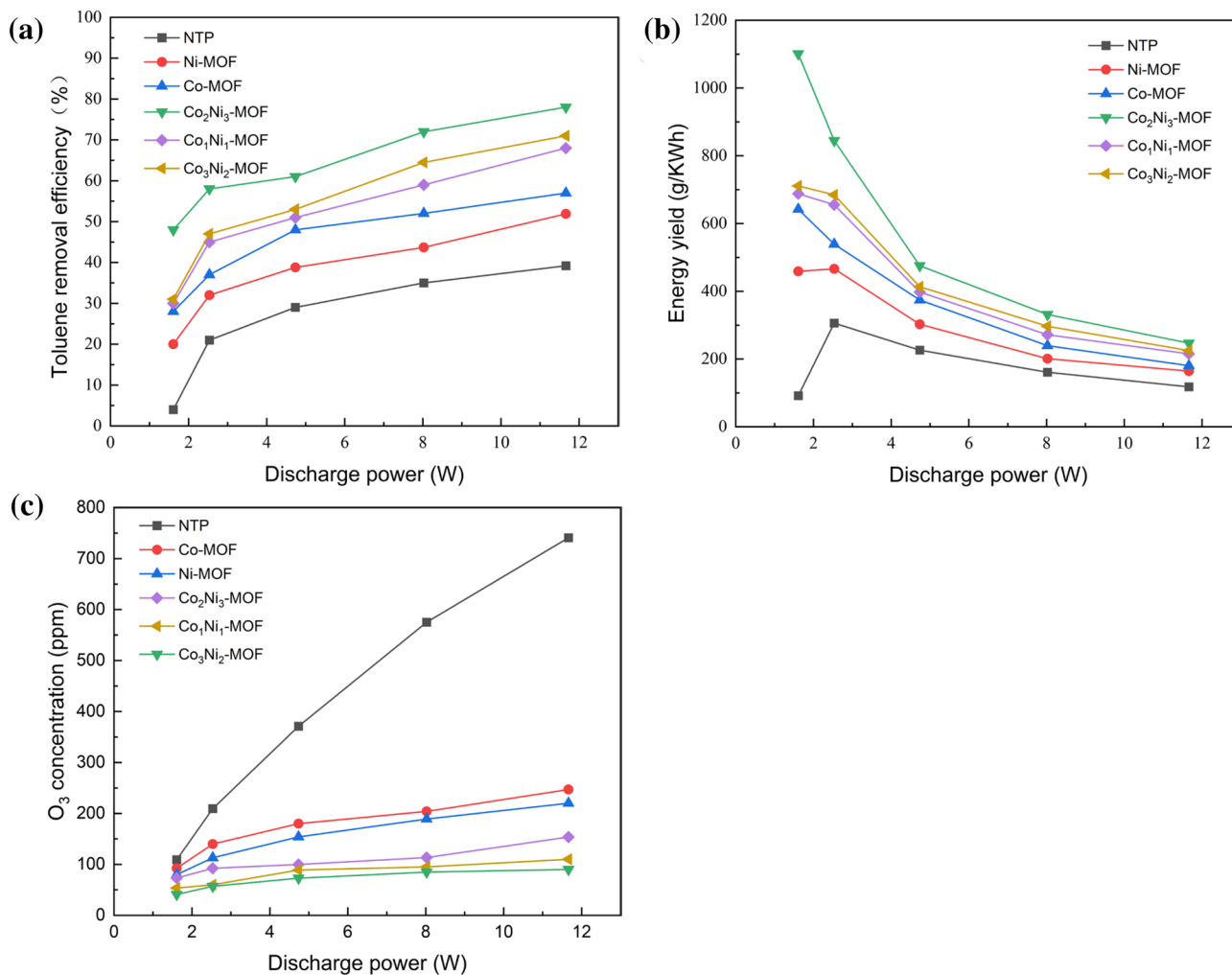
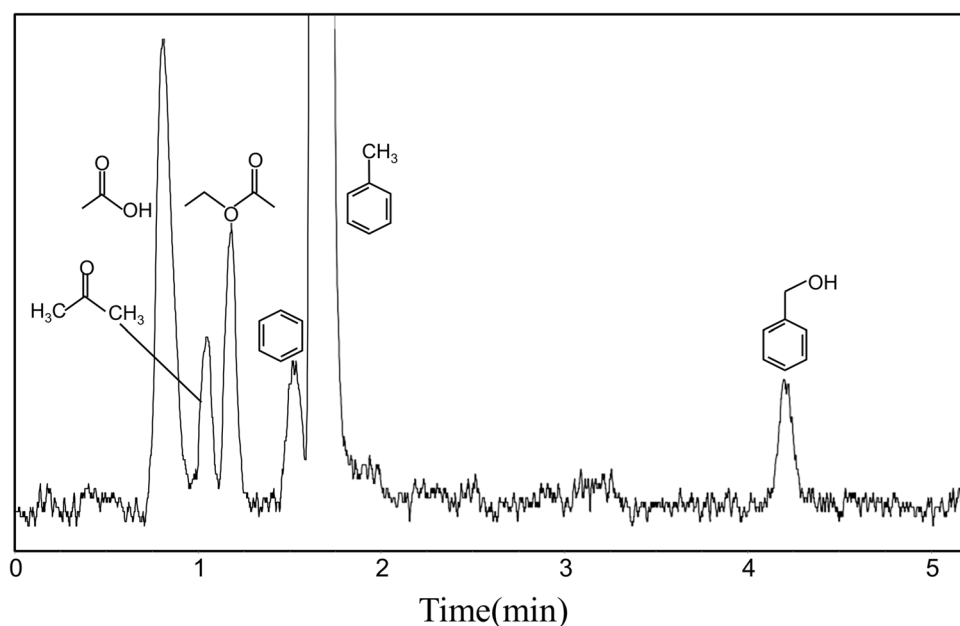
**Fig. 7** The effect of various catalysts on **a** toluene degradation efficiency, **b** energy efficiency and **c** O₃ concentration

Fig. 8 GC spectra of gas-phase by-products in plasma catalysis

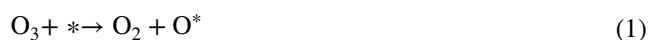
dramatically decreased the amount of gaseous byproducts when compared to the plasma alone. This shows that organic byproducts are extensively mineralized and that the use of a catalyst can convert additional intermediate byproducts into small molecule inorganics.

3.3 Reaction Mechanism

There are two reasons why the MOF-74 catalyst improves toluene removal efficiency in a co-catalytic system. Toluene is cleaved to tiny molecules first by plasma discharge and subsequently degraded by thermal catalytic oxidation of toluene using MOF-74 catalyst. The second is the catalytic oxidation of long reactive radicals and O₃ arrivals produced by plasma discharge with MOF-74 catalyst, which results in the degradation of toluene. However, in our experiments, we discovered that when toluene was degraded by a single plasma, high concentrations of O₃ were detected at the outlet, whereas low concentrations of O₃ were detected at the exhaust gas outlet in a system where toluene was degraded by a plasma in combination with the MOF-74 catalyst. Furthermore, at a catalytic reaction temperature of 200 °C, the MOF-74 catalyst performed poorly or not at all on toluene. We can speculate that the catalyst's catalytic ozone oxidation action is the only thing that could be the reason.

The degradation of the active sites on the surface of MOFs produces additional oxidizing reactive oxygen atoms, which consumes O₃. Further downstream of the discharge zone, reactive oxygen atoms are implicated in the oxidative breakdown of toluene on the surface of MOFs. Simultaneously, the consumption of reactive oxygen atoms accelerates the breakdown of O₃ molecules, resulting in a drop in O₃

concentration at the outflow. The following is the pertinent reaction equation



Based on the above discussion, the degradation mechanism in the plasma-coordinated MOFs catalyst degradation of toluene system can be formally proposed as shown in Fig. 8. On the one hand, the oxidation of toluene on MOFs catalysts is carried out by the Mars-van Krevelen mechanism. In the catalyst-filled region, toluene is adsorbed on the catalyst surface, and the O₃ generated by the plasma reaction decomposes at the oxygen vacancies on the catalyst surface, generating strongly oxidized reactive oxygen species [53]. Reactive oxygen species may be involved in the ring-opening process of benzene rings since toluene and its byproducts undergo extensive oxidation to oxygen-containing intermediates such as acetic acid, acetaldehyde, and ethanol. On the catalyst material, the resultant oxygen-containing intermediates may be further mineralized to CO₂ and H₂O. The oxygen gap is subsequently filled by collecting oxygen molecules in the atmosphere or by capturing oxygen through the breakdown of ozone. As a result, the capacity of O₃ to convert to atomic oxygen may be a crucial factor influencing toluene degradation. On the other hand, toluene oxidation follows the Langmuir–Hinshelwood reaction mechanism. In the Co₂Ni₃-MOF catalyst, the redox cycle of the Co and Ni cations (Co³⁺/Co²⁺ and Ni³⁺/Ni²⁺) replenishes the oxygen

vacancies [54]. Lattice oxygen is consumed via the redox cycle between $\text{Co}^{3+}/\text{Co}^{2+}$ and $\text{Ni}^{3+}/\text{Ni}^{2+}$ to form oxygen vacancies, which then activate gas-phase oxygen to create reactive oxygen species that take part in the oxidation of VOCs [55, 56]. The catalyst for the oxidation of toluene was considerably enhanced in terms of CO_2 selectivity. Applying a heat source to the catalyst can further improve the situation. As a whole, the processes that led to the catalytic oxidation of toluene over $\text{Co}_x\text{Ni}_y\text{-MOF}$ catalysts were mostly of the Mars-van Krevelen and Langmuir–Hinshelwood type (Figs. 9, 10).

The organic by-products from the incomplete toluene degradation would build up on the catalyst surface and cover the active sites, resulting in a decrease in catalytic activity and affecting the degradation effect in the plasma-catalyzed degradation of toluene by MOFs. The toluene removal rate during the 10 h toluene degradation experiments remained stable at around 78%. It demonstrates that MOF can sustain high catalytic activity and does not deactivate when degrading toluene over an extended period of time, and that the catalyst is highly reusable.

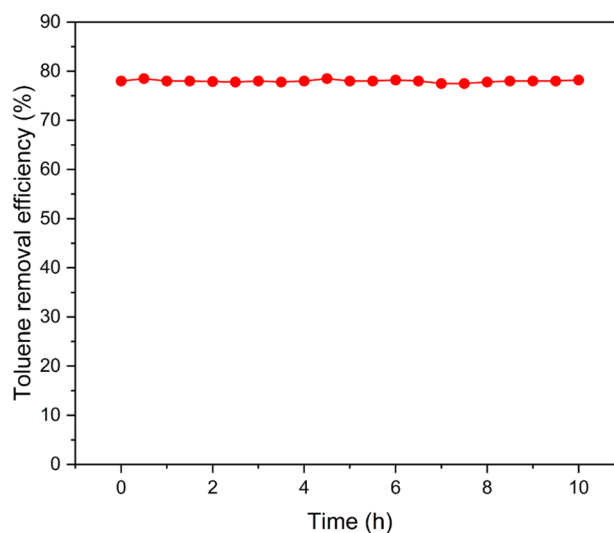
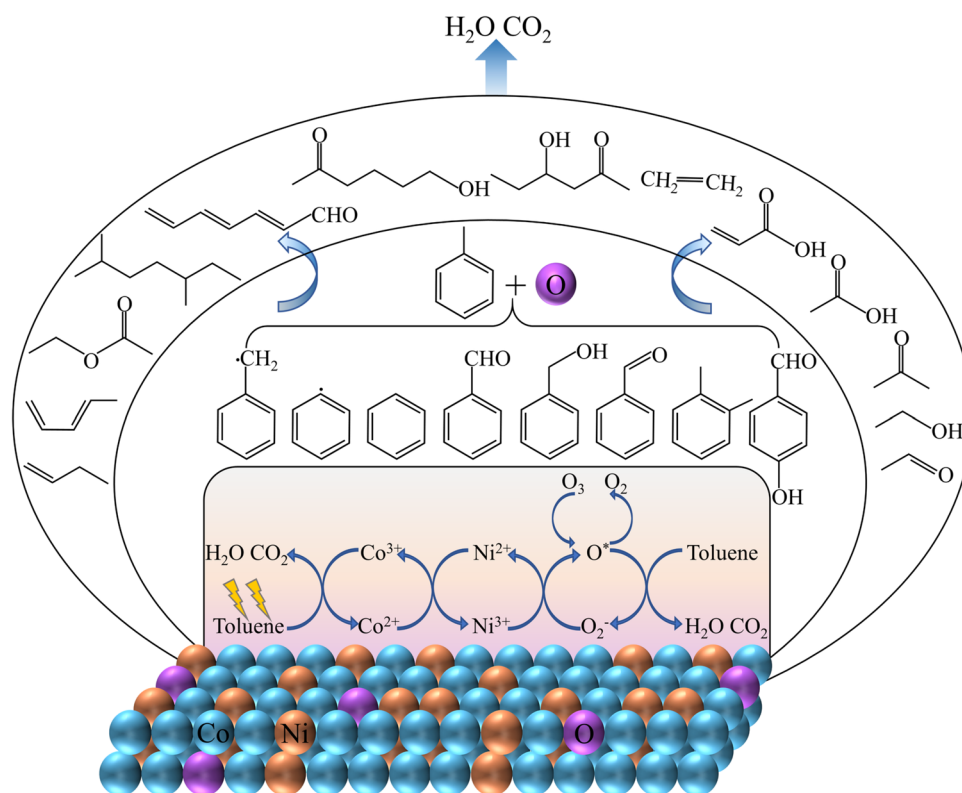


Fig. 10 Catalytic stability test of $\text{Co}_2\text{Ni}_3\text{-MOF}$ catalyst

4 Conclusion

A variety of MOF catalysts with varying Co/Ni ratios were produced hydrothermally and employed in a plasma co-catalytic toluene degradation system in this work. $\text{Co}_2\text{Ni}_3\text{-MOF}$ outperformed the others in terms of catalytic performance

Fig. 9 Degradation mechanism of toluene on the surface of MOF catalyst



and energy efficiency for toluene oxidation. The inflow concentration of toluene was 822.68 mg m⁻³ when the ion discharge power was 11.66 W, and the greatest degradation rate of toluene was 78%, which was 52.3% higher than the single plasma condition. During the 10-h catalyst stability test, the catalytic activity remained steady and efficient. Based on the GC measurement of the reaction tail gas, a putative toluene degradation process over MOFs catalyst was postulated. Toluene ring opening is primarily caused by the synergistic impact of reactive oxygen species and variable metal on the catalyst. This research offers a fresh method for using MOF materials in plasma catalysis to simultaneously and effectively reduce VOC and O₃ pollution.

Acknowledgements This study was supported by the National Key R&D project of China (No. 2018YFC1900203), the National Key R&D project of China (No. 2018YFC1801702),

Declarations

Conflict of interest The authors declare that they have no known competing financial interests or personal relationships that could have appeared to influence the work reported in this paper.

References

- Zhu LL, Shen DK, Luo KH (2020) *J Hazard Mater* 389:122102
- He C, Cheng J, Zhang X, Douthwaite M, Patisson S, Hao ZP (2019) *Chem Rev* 119:4471–4568
- Mu ML, Zhang XF, Yu GQ, Sun CY, Xu RN, Liu N, Wang N, Chen BH, Dai CN (2022) *Sep Purif Technol* 298:121610
- Dong C, Yang JJ, Xie LH, Cui GL, Fang WH, Li JR (2022) *Nat Commun* 13:4991
- Peng YB, Wei X, Wang YJ, Li WW, Zhang SX, Jin J (2022) *ACS Nano* 16:8329–8337
- Li JH, Xiao GF, Guo ZY, Lin BL, Hu Y, Fu ML, Ye DQ (2021) *Chem Eng J* 419:129675
- Dai L, Li XY, Zhang L, Ma PP, Guan J, Yu W (2022) *Adv Compos Hybrid Mater* 5:2285–2296
- Yang ZH, Li J, Liu J, Cao JY, Sheng DH, Cai TJ (2019) *J Environ Manag* 246:71–76
- Youn JS, Bae J, Park S, Park Y-K (2018) *Catal Commun* 113:36–40
- Xiang QS, Fan LM, Li YF, Dong SS, Li K, Bai YH (2022) *Crit Rev Food Sci Nutr* 62:2250–2268
- Chung WC, Mei DH, Tu X, Chang MB (2019) *Catal Rev Sci Eng* 61:270–331
- Yao XM, Jiang N, Li J, Lu N, Shang KF, Wu Y (2019) *Chem Eng J* 362:339–348
- Hossain MM, Mok YS, Nguyen VT, Sosiawati T, Lee B, Kim YJ, Lee JH, Heo I (2022) *Chem Eng Res Des* 177:406–417
- Fan X, Zhu TL, Sun YF, Yan X (2011) *J Hazard Mater* 196:380–385
- Wang JJ, Wang XX, AlQahtani MS, Knecht SD, Bilen SG, Chu W, Song CS (2023) *Chem Eng J* 451:138661
- Kim HH, Teramoto Y, Negishi N, Ogata A (2015) *Catal Today* 256:13–22
- Li G, Jiang X, Lei ZJ, Liu CX, Yang JH, Xu YJ, Xu G (2020) *Sci Rep* 10:13004
- Chen CW, Kosari M, He C, Ma MD, Tian MJ, Jiang ZY, Albilali R (2022) *ACS Appl Mater Interfaces* 14:990–1001
- Hossain MM, Mok YS, Nguyen DB, Kim SJ, Kim YJ, Lee JH, Heo I (2021) *J Hazard Mater* 404:123958
- Qian YT, Zhang FF, Pang H (2021) *Adv Funct Mater* 31:2104231
- Yan XY, Li PX, Song XM, Li JJ, Ren BH, Gao SY, Cao R (2021) *Coord Chem Rev* 443:214034
- Falcaro P, Ricco R, Yazdi A, Imaz I, Furukawa S, Maspoeh D, Ameloot R, Evans JD, Doonan CJ (2016) *Coord Chem Rev* 307:237–254
- Mehtab T, Yasin G, Arif M, Shakeel M, Korai RM, Nadeem M, Muhammad N, Lu X (2019) *J Energy Storage* 21:632–646
- Dhakshinamoorthy A, Asiri AM, Garcia H (2016) *Angewandte Chemie-Int Ed* 55:5414–5445
- Stassen I, Styles M, Greci G, Van Gorp H, Vanderlinden W, De Feyter S, Falcaro P, De Vos D, Vereecken P, Ameloot R (2016) *Abstr Pap Am Chem Soc* 251:5414–5415
- Sun L, Campbell MG, Dinca M (2016) *Angewandte Chemie-Int Ed* 55:3566–3579
- Chen BL, Xiang SC, Qian GD (2010) *Acc Chem Res* 43:1115–1124
- Kitagawa S, Kitaura R, Noro S (2004) *Angewandte Chemie-Int Ed* 43:2334–2375
- Stock N, Biswas S (2012) *Chem Rev* 112:933–969
- Zhang XH, Dong PP, Lee JI, Gray JT, Cha YH, Ha S, Song MK (2019) *Energy Storage Mater* 17:167–177
- Li JT, Xu ZL, Wang T, Xie XW, Li DD, Wang JE, Huang HB, Ao ZM (2022) *Chem Eng J* 448:136900
- Li X, Wang SW, Zhang X, Mei DH, Xu YH, Yu P, Sun YJ (2022) *J Clean Prod* 332:130107
- Guo SH, Qi XJ, Zhou HM, Zhou J, Wang XH, Dong M, Zhao X, Sun CY, Wang XL, Su ZM (2020) *J Mater Chem A* 8:11712–11718
- Zhang XD, Bi FK, Zhu ZQ, Yang Y, Zhao SH, Chen JF, Lv XT, Wang YX, Xu JC, Liu N (2021) *Appl Catal B-Environ* 297:120393
- Rong X, Cao Q, Gao Y, Luan T, Li YT, Man QY, Zhang ZC, Chen BM (2022) *Molecules* 27:7363
- Yi B, Zhao H, Cao L, Si X, Jiang Y, Cheng P, Zuo Y, Zhang Y, Su L, Wang Y, Tsung CK, Chou LY, Xie J (2022) *Materials Today Nano* 17:100158
- Liao L, Ding XG, Li J, Huang LL, Zhang MY, Fan YM, Zhou XB, Zhang YA, Mo SP, Xie QL, Ye DQ (2023) *Sep Purif Technol* 309:122939
- Fu YH, Xu L, Shen HM, Yang H, Zhang FM, Zhu WD, Fan MH (2016) *Chem Eng J* 299:135–141
- Zhou JJ, Ji WX, Xu L, Yang Y, Wang WQ, Ding HL, Xu XC, Wang WW, Zhang PL, Hua ZL, Chen LY (2022) *Chem Eng J* 428:132123
- Wei J, Feng YY, Zhou PP, Liu Y, Xu JY, Xiang R, Ding Y, Zhao CC, Fan LY, Hu CW (2015) *Chemosuschem* 8:2630–2634
- Yuan MW, Yao HQ, Xie LX, Liu XW, Wang H, Islam SM, Shi KR, Yu ZH, Sun GB, Li HF, Ma SL, Kanatzidis MG (2020) *J Am Chem Soc* 142:1574–1583
- Shang YN, Xu X, Gao BY, Ren ZF (2017) *ACS Sustain Chem Eng* 5:8908–8917
- Hao C, Guo YN, Ren WT, Wang XH, Zhu LL, Wang XK, Wu JB (2022) *Electrochim Acta* 412:140135
- Jin XT, Li XL, Lei HT, Guo K, Lv B, Guo HB, Chen DD, Zhang W, Cao R (2021) *J Energy Chem* 63:659–666
- Shi F, Wang ZS, Zhu KY, Zhu XF, Yang WS (2022) *Electrochim Acta* 416:140293
- Lu YX, Guo JL, He ZK, Gao ZD, Song YY, Song YY (2022) *Energy Storage Mater* 48:487–496
- Tian MJ, Guo X, Dong R, Guo Z, Shi JW, Yu YK, Cheng MX, Albilali R, He C (2019) *Appl Catal B-Environ* 259:118018

48. Sun ZH, Mi X, Luo YC, Wang SY, Yuan B, Hao RL, Zhao Y (2021) *ACS Omega* 6:34347–34358
49. Luo YJ, Zheng YB, Zuo JC, Feng XS, Wang XY, Zhang TH, Zhang K, Jiang LL (2018) *J Hazard Mater* 349:119–127
50. Yao X, Li YZ, Fan ZY, Zhang ZX, Chen MX, Shangguan WF (2018) *Ind Eng Chem Res* 57:4214–4224
51. Feng XB, Chen CW, He C, Chai SN, Yu YK, Cheng J (2020) *J Hazard Mater* 383:121143
52. Mustafa MF, Fu XD, Liu YJ, Abbas Y, Wang HT, Lu WJ (2018) *J Hazard Mater* 347:317–324
53. Lei XS, Wang JE, Wang T, Wang XJ, Xie XW, Huang HB, Li DD, Ao ZM (2023) *J Hazard Mater* 456:131671
54. Ji W, Qu GF, Zhou JH, Ning P, Li JY, Tang HM, Pan KH, Xie RS (2023) *Sep Purif Technol* 320:124185
55. Wen M, Dong F, Yao JF, Tang ZC, Zhang JY (2022) *J Catal* 412:42–58
56. Li SJ, Yu X, Dang XQ, Wang PY, Meng XK, Wang Q, Hou H (2022) *J Clean Prod* 340:130774

Publisher's Note Springer Nature remains neutral with regard to jurisdictional claims in published maps and institutional affiliations.

Springer Nature or its licensor (e.g. a society or other partner) holds exclusive rights to this article under a publishing agreement with the author(s) or other rightsholder(s); author self-archiving of the accepted manuscript version of this article is solely governed by the terms of such publishing agreement and applicable law.

Authors and Affiliations

Youxiao Xu^{1,2} · Zhishuncheng Li^{1,2} · Guangfei Qu^{1,2} · Yiting Chen^{1,2} · Huanhuan Wu^{1,2} · Ping Ning^{1,2} · Junyan Li^{1,2}

✉ Ping Ning
ningpinglab@163.com

¹ Faculty of Environmental Science and Engineering,
Kunming University of Science and Technology,
Kunming 650500, Yunnan, China

² National-Regional Engineering Research Center
for Recovery of Waste Gases from Metallurgical
and Chemical Industries-NCW, Kunming 650500, Yunnan,
China